ELSEVIER

Journal of the Mechanics and Physics of Solids
52 (2004) 2431–2454

JOURNAL OF THE
MECHANICS AND
PHYSICS OF SOLIDS

www.elsevier.com/locate/jmps

Size-effects in plane strain sheet-necking

Christian F. Niordson*, Pia Redanz

Department of Mechanical Engineering, Solid Mechanics, Technical University of Denmark, DK-2800 Kgs. Lyngby, Denmark

Received 18 December 2003; received in revised form 13 May 2004; accepted 15 May 2004

Abstract

A finite strain generalization of the strain gradient plasticity theory by Fleck and Hutchinson (J. Mech. Phys. Solids 49 (2001a) 2245) is proposed and used to study size effects in plane strain necking of thin sheets using the finite element method. Both sheets with rigid grips at the ends and specimens with shear free ends are analyzed. The strain gradient plasticity theory predicts delayed onset of localization when compared to conventional theory, and it depresses deformation localization in the neck. The sensitivity to imperfections is analyzed as well as differently hardening materials.

Keywords: Localization; Strain gradient plasticity; Size effects; Finite strain; Elastic–plastic material; Finite elements

1. Introduction

The mechanical properties of thin metal films are important to a variety of technologies, ranging from microelectro-mechanical systems to coatings. For thin sheets or free standing thin films much work has been devoted to experimental determination of mechanical properties (see Huang and Spaepen, 2000; Espinosa et al., 2003). This paper aims at treating the problem of localization of deformation in free standing thin films and sheets using a recent model for plasticity at the micron scale, as well as at giving theoretical predictions which go beyond experimental results reported so far.

On the micron scale, where films are often used, experiments suggest that conventional models for the plastic deformation of metals are insufficient, since they cannot capture observed size-effects (Fleck et al., 1994; Fleck and Hutchinson, 1997; Wei and

* Corresponding author. Tel.: +45-45-25-42-87; fax: +45-45-93-14-75.
E-mail address: cn@mek.dtu.dk (C.F. Niordson).

0022-5096/$ - see front matter © 2004 Elsevier Ltd. All rights reserved.
doi:10.1016/j.jmps.2004.05.009

Hutchinson, 1997; Stölken and Evans, 1998; Begley and Hutchinson, 1998). Hence, more advanced material models have been proposed of which some are based on dislocation mechanics (Deshpande et al., 2003), and others are continuum models, which are able to model relevant size-effects through the incorporation of gradients in the constitutive and equilibrium equations. The continuum models can be subdivided into two classes according to the order of the governing equations. One is termed higher order models by Niordson and Hutchinson (2003b), since these use higher order stresses as work conjugates to gradients of strain and require additional boundary conditions (Aifantis, 1984; Fleck et al., 1994; Fleck and Hutchinson, 1997, 2001a; Gurtin, 2002). The other class is termed lower order models since the theories are based on conventional equilibrium equations, and the only modification compared to conventional theory is the introduction of gradient terms in the hardening relation for the material (Acharya and Bassani, 1996; Bassani, 2001).

Both classes of theories have been used successfully to model a variety of observed size-effects on the micron scale. Some studies have been based on small strain theory to study problems like torsion of thin wires (Fleck et al., 1994), bending of thin beams (Stölken and Evans, 1998), and indentation (Begley and Hutchinson, 1998). Others have used finite strain generalizations to study problems like asymptotic crack tip fields (Hwang et al., 2003), size-effects in fiber-reinforced metals (Niordson and Tvergaard, 2002), and interaction of different size voids (Tvergaard and Niordson, 2004).

The present paper explores the effect of strain gradient hardening on plane strain sheet-necking through studies of the material response and the onset of localization for different combinations of material parameters. Since finite-strain effects are central to the necking problem, a finite strain generalization of the strain gradient plasticity theory by Fleck and Hutchinson (2001a) is proposed. The model is implemented in a finite element code and used to obtain numerical results for the necking problem. The focus of the analyzes is on the influence of the material length parameters on the overall response of thin sheets, the onset of localization, and the development of necks. The sensitivity to imperfections as well as the importance of the aspect ratio of the film are studied. Two types of boundary conditions are investigated. One where the ends are shear free, and another which corresponds to the ends of the film constrained in rigid grips. The numerical results illustrate size-effects, which are important for understanding localization phenomena in micron scale sheets and free standing films.

2. Material model

In this section a finite strain generalization of the strain gradient plasticity theory by Fleck and Hutchinson (2001a) is developed. The initial work is based on a working paper by Fleck and Hutchinson (2001b). An updated Lagrangian formulation based on the work of McMeeking and Rice (1975) and Yamada and Sasaki (1995) for conventional J_2-flow theory is proposed in the present study and used to model the strain gradient effects at finite strains.

Let $\boldsymbol{x}$ and $\boldsymbol{X}$ be the positions of a material point in the reference and in the current configuration respectively. The displacement vector is then given by

$$\boldsymbol{u} = \boldsymbol{X} - \boldsymbol{x} = u_i \boldsymbol{g}_i, \tag{1}$$

where $\boldsymbol{g}_i$ are Cartesian base vectors.

Define the velocity gradient by

$$\dot{\boldsymbol{e}} = \boldsymbol{\nabla} \dot{\boldsymbol{u}} = \frac{\partial \dot{\boldsymbol{X}}}{\partial \boldsymbol{X}} = \dot{\boldsymbol{F}} \cdot \boldsymbol{F}^{-1}, \tag{2}$$

where $\boldsymbol{F} = \partial \boldsymbol{X} / \partial \boldsymbol{x}$ is the deformation gradient. The anti-symmetric part of the velocity gradient is denoted $\dot{\boldsymbol{\omega}}$ and it's components are defined by

$$\dot{\omega}_{ij} = \tfrac{1}{2}(\dot{e}_{ij} - \dot{e}_{ji}) = \tfrac{1}{2}(\dot{u}_{i,j} - \dot{u}_{j,i}). \tag{3}$$

The symmetric part of the velocity gradient is the strain rate, which is taken to be the sum of the elastic and the plastic strain rates

$$\dot{\varepsilon}_{ij} = \tfrac{1}{2}(\dot{e}_{ij} + \dot{e}_{ji}) = \tfrac{1}{2}(\dot{u}_{i,j} + \dot{u}_{j,i}) = \dot{\varepsilon}^E_{ij} + \dot{\varepsilon}^{\mathrm{P}}_{ij}. \tag{4}$$

The gradient measure in the theory by Fleck and Hutchinson (2001a) is based on the following third order tensor ρ_{ijk}, which is the gradient of the plastic strain rate

$$\rho_{ijk} = \rho_{jik} = \dot{\varepsilon}^{\mathrm{P}}_{ij,k}. \tag{5}$$

A measure of effective plastic strain, E^{P}, is used to represent the total dislocation density through the statistically stored dislocations (accounted for in conventional theories through the conventional effective plastic strain, ε^{P}), and geometrically necessary dislocations (included through three invariants, I_1, I_2, and I_3, of homogeneous degree two of ρ_{ijk}). With the usual definition of ε^{P} by the incremental relation $\dot{\varepsilon}^{\mathrm{P}^2} = \frac{2}{3}\dot{\varepsilon}^{\mathrm{P}}_{ij}\dot{\varepsilon}^{\mathrm{P}}_{ij}$, E^{P} is defined by

$$\dot{E}^{\mathrm{P}^2} = \dot{\varepsilon}^{\mathrm{P}^2} + l_1^2 I_1 + 4 l_2^2 I_2 + \frac{8}{3} l_3^2 I_3. \tag{6}$$

Here, l_1, l_2 and l_3 are material length parameters introduced for dimensional consistency. The numerical coefficients of the invariants are chosen such that the material length parameters in the theory have similar meaning as the length parameters in the strain gradient theory of Fleck and Hutchinson (1997), where gradients are introduced through second order gradients of displacement $\eta_{ijk} = u_{i,jk}$.

With σ_{ij} denoting the Cauchy stress tensor, and $\sigma_{(\mathrm{e})} = \sqrt{\frac{3}{2} S_{ij} S_{ij}}$ von Mises' effective stress, where $S_{ij} = \sigma_{ij} - \frac{1}{3}\delta_{ij}\sigma_{kk}$ is the deviatoric stress, we now write the plastic strain rate as the product of its magnitude, $\dot{\varepsilon}^{\mathrm{P}} = \sqrt{\frac{2}{3}\dot{\varepsilon}^{\mathrm{P}}_{ij}\dot{\varepsilon}^{\mathrm{P}}_{ij}}$, and its direction, $m_{ij} = \frac{3}{2} S_{ij}/\sigma_{(\mathrm{e})}$

$$\dot{\varepsilon}^{\mathrm{P}}_{ij} = \frac{3}{2}\frac{S_{ij}}{\sigma_{(\mathrm{e})}}\dot{\varepsilon}^{\mathrm{P}}. \tag{7}$$

This gives the expression for ρ_{ijk}

$$\rho_{ijk} = (m_{ij}\dot{\varepsilon}^{\mathrm{P}})_{,k} = m_{ij,k}\dot{\varepsilon}^{\mathrm{P}} + m_{ij}\dot{\varepsilon}^{\mathrm{P}}_{,k}, \tag{8}$$

which shows how ρ_{ijk} depends on the conventional effective plastic strain and its gradient, as well as on the direction of the plastic strain increment and its gradient, $m_{ij,k}$. Using this relation in the expression for the effective plastic strain (Eq. (6)) gives

$$\dot{E}^{\mathrm{P}^2} = \dot{\varepsilon}^{\mathrm{P}^2} + A_{ij}\dot{\varepsilon}^{\mathrm{P}}_{,i}\dot{\varepsilon}^{\mathrm{P}}_{,j} + B_i\dot{\varepsilon}^{\mathrm{P}}_{,i}\dot{\varepsilon}^{\mathrm{P}} + C\dot{\varepsilon}^{\mathrm{P}^2}, \tag{9}$$

where the tensors A_{ij}, B_i and C depend on the three material length parameters l_1, l_2, and l_3 as well as on the spatial gradients of the plastic strain increment direction (for details see Fleck and Hutchinson, 2001a).

Within the framework of the present theory, a single parameter theory closely related to the strain gradient theory of Aifantis (1984) can be formulated. This is done by defining the measure of the effective plastic strain as

$$\dot{E}^{\mathrm{P}^2} = \dot{\varepsilon}^{\mathrm{P}^2} + l_*^2\dot{\varepsilon}^{\mathrm{P}}_{,i}\dot{\varepsilon}^{\mathrm{P}}_{,i}, \tag{10}$$

where l_* is a new material length parameter (Fleck and Hutchinson, 2001a).

2.1. Principle of virtual work in the current configuration

The finite strain generalization of the strain gradient plasticity theory is based on the following form of the principle of virtual work:

$$\int_V (\sigma_{ij}\delta\dot{\varepsilon}_{ij} + (Q - \sigma_{(\mathrm{e})})\delta\dot{\varepsilon}^{\mathrm{P}} + \tau_i\delta\dot{\varepsilon}^{\mathrm{P}}_{,i})\,\mathrm{d}V = \int_S (T_i\delta\dot{u}_i + t\delta\dot{\varepsilon}^{\mathrm{P}})\,\mathrm{d}S, \tag{11}$$

which can be expressed in index-free notation as

$$\int_V (\boldsymbol{\sigma} : \delta\dot{\boldsymbol{\varepsilon}} + (Q - \sigma_{(\mathrm{e})})\delta\dot{\varepsilon}^{\mathrm{P}} + \boldsymbol{\tau}\cdot\delta\boldsymbol{\nabla}\dot{\varepsilon}^{\mathrm{P}})\,\mathrm{d}V = \int_S (\boldsymbol{T}\cdot\delta\dot{\boldsymbol{u}} + t\delta\dot{\varepsilon}^{\mathrm{P}})\,\mathrm{d}S. \tag{12}$$

Here, Q is the generalized effective stress, τ_i is the higher order stress which is work-conjugate to the gradient of the effective plastic strain $\varepsilon^{\mathrm{P}}_{,i}$, T_i is the traction, and finally, t is the higher order traction. The current volume and surface are denoted V and S, respectively.

Using Gauss's theorem and rewriting the principle of virtual work, which must hold for arbitrary variations of $\dot{u}_i$ and $\dot{\varepsilon}^{\mathrm{P}}$, the strong form of the field equations is found. First, the conventional equilibrium and boundary conditions, and additionally the consistency condition

$$Q - \sigma_{(\mathrm{e})} - \tau_{i,i} = 0 \tag{13}$$

and the higher order boundary condition

$$t = \tau_i N_i, \tag{14}$$

which must be fulfilled at the boundary of the plastic parts of the solid. Here, N_i is the surface unit normal in the current configuration.

2.2. Going from the current frame to the reference configuration

To obtain an expression for the principle of virtual work in the reference configuration, we now define Kirchhoff stress measures as follows (defining $J = \det \boldsymbol{F}$)

$$\boldsymbol{\varsigma} = J\boldsymbol{\sigma}, \quad \varsigma_{ij} = J\sigma_{ij}, \tag{15}$$

$$\sigma^{\varsigma}_{(\mathrm{e})} = J\sigma_{(\mathrm{e})}, \tag{16}$$

$$\boldsymbol{\rho} = J\boldsymbol{\tau}, \quad \rho_i = J\tau_i, \tag{17}$$

$$q = JQ \tag{18}$$

and first Piola–Kirchhoff stress measures as

$$\boldsymbol{s} = J\boldsymbol{F}^{-1} \cdot \boldsymbol{\sigma} = \boldsymbol{F}^{-1} \cdot \boldsymbol{\varsigma}, \tag{19}$$

$$\boldsymbol{\varrho} = J\boldsymbol{F}^{-1} \cdot \boldsymbol{\tau} = \boldsymbol{F}^{-1} \cdot \boldsymbol{\rho}. \tag{20}$$

Introducing the Piola–Kirchhoff measures into the principle of virtual work Eq. (12) gives

$$\int_{V_0} (\boldsymbol{s} : \delta\dot{\boldsymbol{F}} + (q - \sigma^{\varsigma}_{(\mathrm{e})})\delta\dot{\varepsilon}^{\mathrm{P}} + \boldsymbol{\varrho} \cdot \delta\boldsymbol{\nabla}_0\dot{\varepsilon}^{\mathrm{P}})\,\mathrm{d}V_0 = \int_{S_0} (\boldsymbol{T}_0 \cdot \delta\dot{\boldsymbol{u}} + t_0\delta\dot{\varepsilon}^{\mathrm{P}})\,\mathrm{d}S_0,$$

where subscript "0" refers to the reference configuration and

$$\boldsymbol{T}_0 = \boldsymbol{n} \cdot \boldsymbol{s} = \boldsymbol{s}^{\mathrm{T}} \cdot \boldsymbol{n}, \tag{21}$$

$$t_0 = \boldsymbol{n} \cdot \boldsymbol{\varrho} \tag{22}$$

are the nominal traction and the nominal higher order traction, respectively. In these expressions $\boldsymbol{n}$ is the surface unit normal in the reference configuration, which can be expressed by the unit normal in the deformed configuration through Nanson's relation

$$\boldsymbol{N}\,\mathrm{d}S = J\boldsymbol{n} \cdot \boldsymbol{F}^{-1}\,\mathrm{d}S_0. \tag{23}$$

2.3. Incremental principle of virtual work

The incremental version of the principle of virtual work can now be expressed as

$$\int_{V_0} (\dot{\boldsymbol{s}} : \delta\dot{\boldsymbol{F}} + (\dot{q} - \dot{\sigma}^{\varsigma}_{(\mathrm{e})})\delta\dot{\varepsilon}^{\mathrm{P}} + \dot{\boldsymbol{\varrho}} \cdot \delta\boldsymbol{\nabla}_0\dot{\varepsilon}^{\mathrm{P}})\,\mathrm{d}V_0 = \int_{S_0} (\dot{\boldsymbol{T}}_0 \cdot \delta\dot{\boldsymbol{u}} + \dot{t}_0\delta\dot{\varepsilon}^{\mathrm{P}})\,\mathrm{d}S_0. \tag{24}$$

In index notation, the incremental version of the principle of virtual work is then

$$\int_{V_0} (\dot{s}_{ij}\delta\dot{F}_{ji} + (\dot{q} - \dot{\sigma}^{\varsigma}_{(\mathrm{e})})\delta\dot{\varepsilon}^{\mathrm{P}} + \dot{\varrho}_i\delta\dot{\varepsilon}^{\mathrm{P}}_{0,i})\,\mathrm{d}V_0 = \int_{S_0} (\dot{T}_{0i}\delta\dot{u}_i + \dot{t}_0\delta\dot{\varepsilon}^{\mathrm{P}})\,\mathrm{d}S_0. \tag{25}$$

Aiming at formulating the constitutive relation in the Jaumann rate (denoted $\overset{\triangledown}{()}$) of the Kirchhoff stress and the convected rate (denoted $\overset{\vee}{()}$) of the higher order Kirchhoff

stress, the first Piola–Kirchhoff stress measures are expressed as

$$\dot{s}_{ij} = \overset{\triangledown}{\varsigma}_{ij} - \sigma_{kj}\dot{\varepsilon}_{ik} - \sigma_{ik}\dot{\varepsilon}_{jk} + \sigma_{ik}\dot{e}_{jk}, \tag{26}$$

$$\dot{\varrho}_i = \overset{\vee}{\rho}_i. \tag{27}$$

Here, it is exploited that within an updated Lagrangian framework the reference configuration coincides with the current configuration, and hence $\boldsymbol{F} = \boldsymbol{I}$ and $J = 1$.

Using the above equations to rewrite the left-hand side of Eq. (25), the incremental version of the principle of virtual work is expressed as

$$\begin{aligned}\int_V (\overset{\triangledown}{\varsigma}_{ij}\delta\dot{\varepsilon}_{ij} - \sigma_{ij}(2\dot{\varepsilon}_{ik}\delta\dot{\varepsilon}_{kj} - \dot{e}_{kj}\delta\dot{e}_{ki}) + (\dot{q} - \dot{\sigma}^{\varsigma}_{(\mathrm{e})})\delta\dot{\varepsilon}^{\mathrm{P}} + \overset{\vee}{\rho}_i\delta\dot{\varepsilon}^{\mathrm{P}}_{0,i})\,\mathrm{d}V \\ = \int_S (\dot{T}_{0i}\delta\dot{u}_i + \dot{t}_0\delta\dot{\varepsilon}^{\mathrm{P}})\,\mathrm{d}S - \left[\int_V (\sigma_{ij}\delta\dot{\varepsilon}_{ij} + (Q - \sigma_{(\mathrm{e})})\delta\dot{\varepsilon}^{\mathrm{P}} + \tau_i\delta\dot{\varepsilon}^{\mathrm{P}}_{0,i})\,\mathrm{d}V \right. \\ \left. - \int_S (T_{0i}\delta\dot{u}_i + t_0\delta\dot{\varepsilon}^{\mathrm{P}})\,\mathrm{d}S\right],\end{aligned} \tag{28}$$

which is, when excluding the higher order terms, identical to expressions derived in McMeeking and Rice (1975) and Yamada and Sasaki (1995). The term in the square brackets is the equilibrium correction term, which is included to ensure that the incremental solution does not drift away from equilibrium.

2.4. Constitutive equations

The finite strain generalization of the constitutive equations for the stress-measures corresponding to the total strain, the plastic strain, and the plastic strain gradient, respectively, are proposed as

$$\overset{\triangledown}{\varsigma}_{ij} = \mathscr{R}_{ijkl}(\dot{\varepsilon}_{kl} - \dot{\varepsilon}^{\mathrm{P}}m_{kl}) = \dot{\varsigma}_{ij} - \dot{\omega}_{ik}\sigma_{kj} - \sigma_{ik}\dot{\omega}_{jk}, \tag{29}$$

$$\dot{q} - \dot{\sigma}^{\varsigma}_{(\mathrm{e})} = h\left(\dot{\varepsilon}^{\mathrm{P}} + \frac{1}{2}B_i\dot{\varepsilon}^{\mathrm{P}}_{,i} + C\dot{\varepsilon}^{\mathrm{P}}\right) - m_{ij}\overset{\triangledown}{\varsigma}_{ij}, \tag{30}$$

$$\overset{\vee}{\rho}_i = h(A_{ij}\dot{\varepsilon}^{\mathrm{P}}_{,j} + \frac{1}{2}B_i\dot{\varepsilon}^{\mathrm{P}}) = \dot{\rho}_i - \dot{e}_{ik}\rho_k, \tag{31}$$

where

$$\mathscr{R}_{ijkl} = \frac{E}{1+v}\left(\frac{1}{2}(\delta_{ik}\delta_{jl} + \delta_{il}\delta_{jk}) + \frac{v}{1-2v}\,\delta_{ij}\delta_{kl}\right) \tag{32}$$

and the hardening modulus is given by

$$h[E^{\mathrm{P}}] = \left(\frac{1}{E_{\mathrm{t}}[E^{\mathrm{P}}]} - \frac{1}{E}\right)^{-1}. \tag{33}$$

Here, E_{t} is the tangent modulus and it is noted that the hardening modulus is evaluated at E^{P} rather than at ε^{P} as it would be in a conventional theory.

The constitutive equation for the generalized effective stress in Eq. (30) can also be expressed by

$$\dot{q} = h\left(\dot{\varepsilon}^{\mathrm{P}} + \frac{1}{2} B_i \dot{\varepsilon}^{\mathrm{P}}_{,i} + C\dot{\varepsilon}^{\mathrm{P}}\right) \tag{34}$$

since $\dot{\sigma}^{\varsigma}_{(\mathrm{e})} = m_{ij} \overset{\triangledown}{\varsigma}_{ij}$.

Instead of using the convected rate for the higher order stress in the constitutive equations (Eq. (31)), one could use the Jaumann rate,

$$\overset{\triangledown}{\rho}_i = h(A_{ij}\dot{\varepsilon}^{\mathrm{P}}_{,j} + \frac{1}{2} B_i \dot{\varepsilon}^{\mathrm{P}}) = \dot{\rho}_i - \dot{\omega}_{ik}\rho_k. \tag{35}$$

This constitutes a different constitutive assumption, which employed in the principle of virtual work, Eq. (25), leads to a non-symmetric stiffness matrix, which is not the case when using the convected rate in the constitutive equation for the higher order stress. For the sake of simplicity, we will proceed with using the convected rate for the higher order stress (Eq. (31)).

3. Problem formulation and numerical method

A rectangular sheet under plane strain tension is considered (see Fig. 1). The initial width and length of the sheet is $2a_0$ and $2b_0$, respectively, and it has a cosine imperfection of magnitude δ_0. As load is applied to the sheet, it is elongated, and the magnitude of the neck δ changes. Due to the geometrical changes of the specimen, the nominal stress passes through a maximum, and at some point thereafter elastic unloading begins; this is defined as the onset of localization. After this point, the neck grows rapidly, and soon after all plastic deformation takes place in a narrow band around the midpoint of the specimen.

The numerical solutions are obtained using a special kind of finite element method where nodal effective plastic strain increments, $\dot{\varepsilon}^{\mathrm{P}}_n$, appear directly as unknowns on equal footing with the nodal displacement increments, $\dot{D}^{\mathrm{n}}$. The structure of the finite element method as it is used in the present study has been used by Vardoulakis and Aifantis (1991), de Borst and Mühlhaus (1992), and de Borst and Pamin (1996), to model the gradient theory by Aifantis (1984), and by Niordson and Hutchinson (2003a) to model the small strain theory by Fleck and Hutchinson (2001a).

The displacement increments, $\dot{u}_i$, and the effective plastic strain increments, $\dot{\varepsilon}^{\mathrm{P}}$, are interpolated within each element between the nodal displacement increments, $\dot{D}^{\mathrm{n}}$, and the nodal effective plastic strain increments, $\dot{\varepsilon}^{\mathrm{P}}_n$, respectively

$$\dot{u}_i = \sum_{n=1}^{2k} N^n_i \dot{D}^{\mathrm{n}}, \qquad \dot{\varepsilon}^{\mathrm{P}} = \sum_{n=1}^{l} M^n \dot{\varepsilon}^{\mathrm{P}}_n. \tag{36}$$

Here, N^n_i and M^n are shape functions, and k and l are the number of nodes used for the displacement interpolation and the effective plastic strain interpolation, respectively. A linear interpolation of both the displacements and the effective plastic strain is used

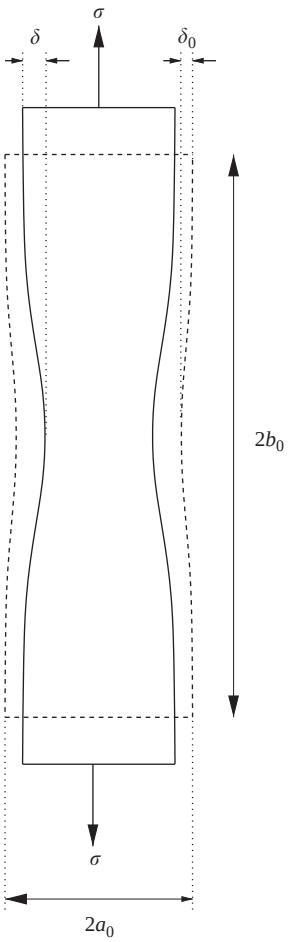

Fig. 1. The geometry of the specimen in the undeformed configuration (dashed line) and in the deformed state (solid line). The amplitude of the neck is denoted δ, and it has the value δ_0 in the undeformed configuration.

which means that $k = l = 3$ in the above equations. The appropriate derivatives of the displacement field and the effective plastic strain field can be expressed as

$$\dot{e}_{ij} = \sum_{n=1}^{2k} N^n_{i,j}\dot{D}^{\mathrm{n}}, \quad \dot{\varepsilon}_{ij} = \sum_{n=1}^{2k} E^n_{ij}\dot{D}^{\mathrm{n}}, \quad \dot{\varepsilon}^{\mathrm{P}}_{,i} = \sum_{n=1}^{l} M^n_{,i}\dot{\varepsilon}^{\mathrm{P}}_n \tag{37}$$

with

$$E^n_{ij} = \tfrac{1}{2}(N^n_{i,j} + N^n_{j,i}). \tag{38}$$

Using these relations in the principle of virtual work (Eq. (28)) which must hold for arbitrary variations of $\delta\dot{D}^{\mathrm{n}}$ and $\delta\dot{\varepsilon}^{\mathrm{P}}_n$, we can now write the discretized equations in

the following form:

$$\begin{bmatrix} \boldsymbol{K}_e & \boldsymbol{K}_{ep} \\ \boldsymbol{K}_{ep}^T & \boldsymbol{K}_p \end{bmatrix} \begin{bmatrix} \dot{\boldsymbol{D}} \\ \dot{\boldsymbol{\varepsilon}}^P \end{bmatrix} = \begin{bmatrix} \dot{\boldsymbol{F}}_1 \\ \dot{\boldsymbol{F}}_2 \end{bmatrix} + \begin{bmatrix} \boldsymbol{C}_1 \\ \boldsymbol{C}_2 \end{bmatrix}, \tag{39}$$

where

$$\boldsymbol{K}_e^{nm} = \int_{V_0} (E_{ij}^n \mathscr{R}_{ijkl} E_{kl}^m + \sigma_{ij}(N_{k,j}^m N_{k,i}^n - 2E_{ik}^m E_{kj}^n)) \, \mathrm{d}V_0 \tag{40}$$

is the elastic stiffness matrix,

$$\boldsymbol{K}_{ep}^{nm} = -\int_{V_0} (E_{ij}^n \mathscr{R}_{ijkl} m_{kl} M^m) \, \mathrm{d}V_0 \tag{41}$$

is a matrix of dimension force, and

$$\begin{aligned} \boldsymbol{K}_p^{nm} = \int_{V_0} (& m_{ij} \mathscr{R}_{ijkl} m_{kl} M^m M^n + h(M^m M^n + A_{ij} M_{,j}^m M_{,i}^n \\ & + \tfrac{1}{2} B_i (M_{,i}^m M^n + M^m M_{,i}^n) + C M^m M^n)) \, \mathrm{d}V_0 \end{aligned} \tag{42}$$

is a matrix of dimension energy.

The first part of the right-hand side of Eq. (39) consists of two components,

$$\dot{\boldsymbol{F}}_1^n = \int_{S_0} \dot{T}_{0i} N_i^n \, \mathrm{d}S_0, \tag{43}$$

which is the conventional external incremental force vector, and

$$\dot{\boldsymbol{F}}_2^n = \int_{S_0} \dot{t}_0 M^n \, \mathrm{d}S_0, \tag{44}$$

which is the incremental higher order force vector.

In order to guarantee total equilibrium, the equilibrium correction term should be added to the right-hand side of the system of equations as shown in Eq. (28). The vector to be added has two parts, one affecting displacement degrees of freedom $\boldsymbol{C}_1$, which must be added to $\dot{\boldsymbol{F}}_1$, and another affecting the effective plastic strain degrees of freedom $\boldsymbol{C}_2$, which must be added to $\dot{\boldsymbol{F}}_2$. The equilibrium correction vectors are calculated as follows:

$$\boldsymbol{C}_1^n = -\int_V \sigma_{ij} E_{ij}^n \, \mathrm{d}V + \int_S T_{0i} N_i^n \, \mathrm{d}S, \tag{45}$$

$$\boldsymbol{C}_2^n = -\int_V ((Q - \sigma_{(\mathrm{e})}) M^n + \tau_i M_{,i}^n) \, \mathrm{d}V + \int_S t_0 M^n \, \mathrm{d}S. \tag{46}$$

When the nodal displacement and effective plastic strain increments have been determined, the elastic strains are calculated, and then the Jaumann rate of the stress and the convected rate of the higher order stress can be found according to Eqs. (29)

and (31). The increments of the stress tensor and the higher order stress vector are then calculated by

$$\dot{\sigma}_{ij} = \overset{\nabla}{\varsigma}_{ij} + \dot{\omega}_{ik}\sigma_{kj} + \sigma_{ik}\dot{\omega}_{jk} - \sigma_{ij}\dot{\varepsilon}_{kk}, \tag{47}$$

$$\dot{\tau}_i = \overset{\vee}{\rho}_i + \dot{e}_{ik}\tau_k - \tau_i\dot{\varepsilon}_{kk}, \tag{48}$$

where the expression for the stress increments, Eq. (47), can also be found in Yamada and Sasaki (1995).

Initial plastic yielding is initiated when $\sigma_{(e)}$ becomes larger than the initial yield stress, σ_y. Unloading of an integration point within an element along the elastic moduli is started, when the solution has found a negative increment of the effective plastic strain at that integration point in the previous increment. After elastic unloading plastic yielding is restarted when Q reaches Q_y. The present strain gradient plasticity theory reduces to J_2-finite strain theory when all material length parameters are set to zero.

The meshes used in the present study are rectangular with quadrilateral elements each subdivided by the diagonals into four triangles. In order to avoid spurious modes for the incremental effective plastic strain field (see e.g. de Borst and Pamin, 1996), a three point integration rule is needed for the integration of $\boldsymbol{K}_{\boldsymbol{p}}^{nm}$. In the present work, we have used a three point integration rule for all integrations (40)–(42) and (45)–(46) in order to obtain consistency between the discretized incremental principle of virtual work and the equilibrium correction term.

Numerical tests showed that the results in the present work are independent of the boundary condition at the elastic-plastic boundary. Whether the plastic flow rate is constrained, $\dot{\varepsilon}^{\mathrm{P}} = 0$, or the higher order traction rate is set to zero, $\dot{\tau}_i n_i = 0$, makes no significant difference.

In the present numerical implementation of the material model it has been found that good convergence is obtained for a material with linear hardening. The results to be presented here apply linear hardening.

A more detailed description of the computational and modeling details for the small strain version of the present theory (Fleck and Hutchinson, 2001a) has been given by Niordson and Hutchinson (2003a). Most details are similar in the finite strain case and will not be repeated here.

4. Results

The numerical results presented in this section focus on the influence of the material length parameters on the overall stress–strain response of specimens with different material parameters and geometries. The geometry is specified by two parameters; the aspect ratio, b_0/a_0, and the amplitude of the imperfection normalized by the half width of the specimen, δ_0/a_0, see Fig. 1. In addition to the material length parameters, the material is defined according to the conventional material parameters, Young's modulus, E, Poisson's ratio, ν, the initial yield stress, σ_y, and the tangent modulus, E_{t}. Unless otherwise is stated plane strain specimens with shear free ends are studied using

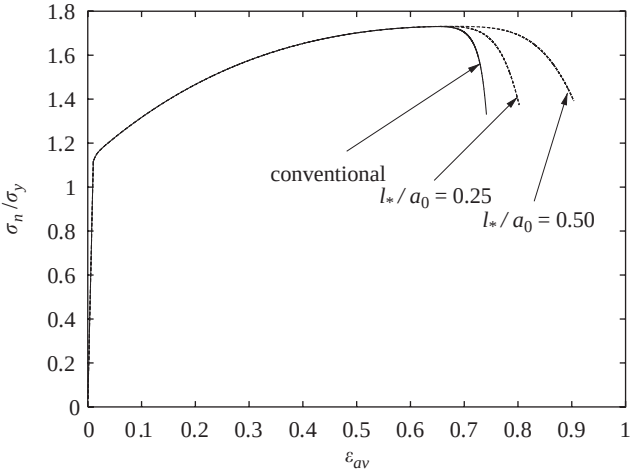

Fig. 2. Overall response for specimens with shear free ends characterized by the geometrical parameters $b_0/a_0 = 3.0$, and $\delta_0/a_0 = 5.0 \times 10^{-3}$, and the material parameters $\sigma_y/E = 0.01$, $\nu = 0.3$, and $E_t/E = 1/40$. The solid curve shows results for a conventional material, while the two dashed curves show results for materials with $l_*/a_0 = 0.25$ and $l_*/a_0 = 0.50$.

the following material parameters:

$$b_0/a_0 = 3, \quad \delta_0/a_0 = 0.005, \tag{49}$$

$$\sigma_y/E = 0.01, \quad \nu = 0.3, \quad E_t/E = 1/40. \tag{50}$$

Due to symmetry only a quarter of the specimen is modeled by dividing it into 25 quadrilateral elements through the half width of the sheet, and 150 elements along the half length of the sheet. For specimens with different aspect ratios than $b_0/a_0 = 3$ the number of elements along the length of the specimen is scaled properly, so that the elements in the neck have the same aspect ratios.

Fig. 2 shows the nominal stress in the tensile direction normalized by the yield stress in uniaxial tension, as a function of the average logarithmic strain in the tensile direction, ε_{av}. The solid curve shows the results for a conventional material, while the dashed curves show results for gradient dependent materials modeled by the single parameter theory (Eq. (10)) with two different values of the material length parameter. Since the stress and strain state are almost constant throughout the solid until the maximum load point is reached, gradient hardening has no significant effect on the material response before the maximum, which is illustrated through the coinciding curves of the overall response in Fig. 2. On the other hand at some point after the maximum load point the response is significantly affected by the material length parameter, since localization of the solid leads to significant strain gradients and thereby differences in gradient hardening. In the figure this is seen through the increased stiffness for increasing length parameters toward the end of the curves. Analyzes in Fig. 2 (and in the following figures as well) are terminated at a critical value of the aspect ratio of the

Table 1
The average strain at maximum load, ε^{m}, and at the onset of localization, ε^{l}, are shown together with the delay of the onset of localization, $\varepsilon^{\mathrm{l}} - \varepsilon^{\mathrm{m}}$, for a conventional material and different gradient dependent materials

	ε^{m}	ε^{l}	$\varepsilon^{\mathrm{l}} - \varepsilon^{\mathrm{m}}$
Conventional	0.651	0.654	0.003
$l_*/a_0 = 0.25$	0.664	0.673	0.010
$l_*/a_0 = 0.50$	0.677	0.722	0.045
$l_1/a_0 = 0.50$	0.677	0.718	0.041
$l_2/a_0 = 0.50$	0.673	0.708	0.035
$l_3/a_0 = 0.50$	0.674	0.719	0.045

The specimens have shear free ends, and the geometry of the specimens is characterized by $b_0/a_0 = 3.0$ and $\delta_0/a_0 = 5.0 \times 10^{-3}$, and the conventional material parameters are $\sigma_y/E = 0.01$, $\nu = 0.3$, and $E_t/E = 1/40$.

elements in the numerical model. The quadrilaterals in the neck start out by having an aspect ratio of 0.2, and the analyzes are terminated when the aspect ratio reaches 10, which corresponds to stopping the analyzes when the accumulated effective strain in the neck has reached around 2.25. It is seen that while the nominal stress at the end of the analyzes is almost independent of the gradient effects, the strain is very much influenced by the material length parameter. Hence, at the end of the analyzes, the overall strain is around 22% larger for the material with $l_*/a_0 = 0.50$ compared to the conventional material. The increased stiffness for the gradient dependent materials can be attributed to gradient hardening and thereby to the decreased tendency to localization for the gradient dependent materials. This is furthermore illustrated in Table 1, which shows the average logarithmic strain at the maximum load point, ε^{m}, and at the onset of localization (defined as the onset of elastic unloading), ε^{l}, for the different materials discussed in relation to Fig. 2. The third column shows the delay of the onset of localization compared to the maximum load point, calculated as the difference in average logarithmic strain, $\varepsilon^{\mathrm{l}} - \varepsilon^{\mathrm{m}}$. The table shows that the delay of elastic unloading compared to the maximum load point is rather small for the conventional material, and that it increases significantly with the material length parameter, l_*. Hence, for the conventional material the delay of the onset of localization is around 0.003, while it is around 15 times larger for the material characterized by $l_*/a_0 = 0.50$.

Experiments suggest that the material length parameter valid for most metals is on the order of a micron (see e.g. Hutchinson, 2000; Fleck and Hutchinson, 2001a). This implies that the specimen with $l_*/a_0 = 0.5$ in Fig. 2 has a width on the order of 10 μm.

Fig. 3 shows the deformed geometries of the sheets analyzed in Fig. 2 at the end of the simulations. In the figure both the undeformed meshes, and the deformed meshes are shown. The black area marks the part of the material that is being deformed plastically, while the rest of the material is unloading elastically. Keeping in mind that the criterion for ending the simulations is tied to a critical value of the effective strain within the neck, it is seen that the overall deformation increases with increasing material length scale for this criterion to be met. Furthermore, the figure shows that

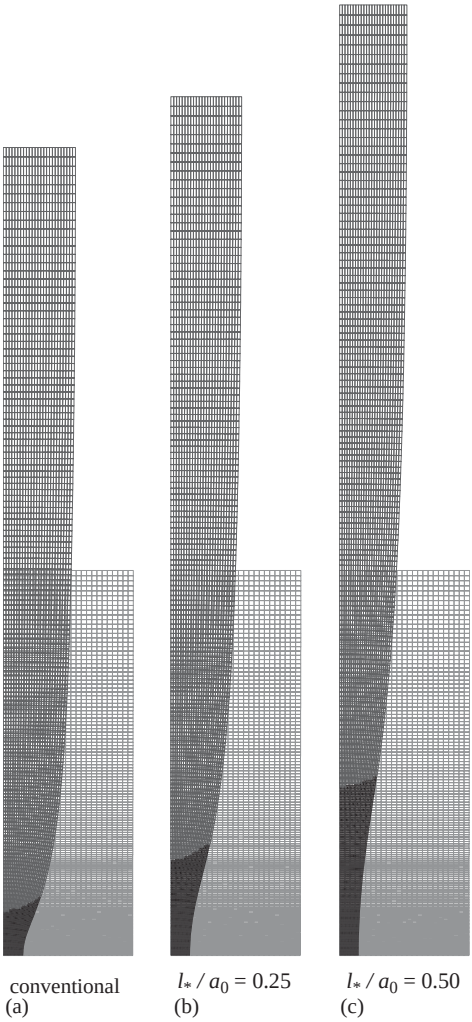

Fig. 3. Deformed geometries for specimens with shear free ends characterized by the geometrical parameters $b_0/a_0 = 3.0$ and $\delta_0/a_0 = 5.0 \times 10^{-3}$, and the material parameters $\sigma_y/E = 0.01$, $\nu = 0.3$, and $E_t/E = 1/40$, at the end of the simulations. Figure (a) shows the deformed geometry for a conventional material, and the figures (b) and (c) show the deformed geometries for gradient dependent materials with $l_*/a_0 = 0.25$ and $l_*/a_0 = 0.50$, respectively. The black areas show the zones that are being plastically loaded, while the rest is being elastically unloaded.

for the gradient dependent materials the active plastic zone is significantly longer than for the conventional material, and that the neck becomes more smooth for increasing values of l_*.

The influence of the material length parameter on the development of the neck is shown in Fig. 4. In this figure the amplitude of the neck normalized by the initial

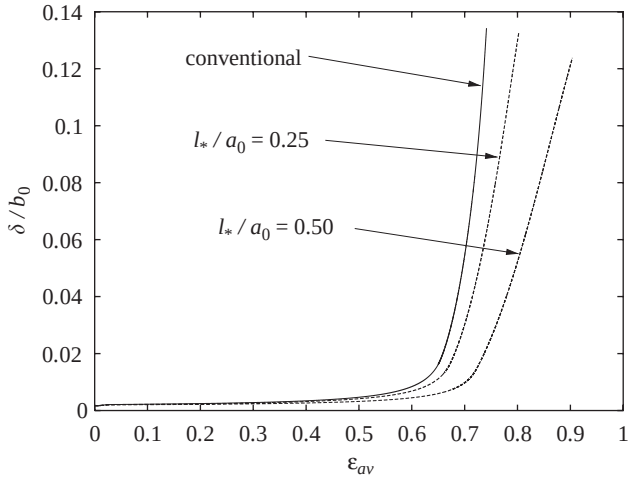

Fig. 4. Development of the neck for specimens with shear free ends characterized by the geometrical parameters $b_0/a_0 = 3.0$ and $\delta_0/a_0 = 5.0 \times 10^{-3}$, and the material parameters $\sigma_y/E = 0.01$, $\nu = 0.3$, and $E_t/E = 1/40$. The solid curve shows results for a conventional material, while the two dashed curves show results for materials with $l_*/a_0 = 0.25$ and $l_*/a_0 = 0.50$.

length of the specimen is shown as a function of the average strain. It is seen that for all values of the overall deformation, the amplitude of the neck decreases for increasing values of the material length parameter. Hence, gradient hardening limits localization.

Until now, only the single parameter theory has been discussed. In Fig. 5 the solid curve shows the response for a conventional material, and the dashed curve shows the response for a gradient dependent material characterized by $l_*/a_0 = 0.50$. The three dotted curves represent responses for materials characterized by the multi parameter theory with each of the three length parameters set equal to $a_0/2$ one by one. The figure illustrates that it is not significant for the present problem which of the theories and which of the three length parameters is used. In Table 1 the average logarithmic strain at the maximum load point and at the onset of localization are shown for the materials discussed in relation to Fig. 5. The table shows that for all the gradient dependent materials the maximum load point is reached at a strain of 0.67–0.68, and that the onset of localization is delayed between 0.035 and 0.045 compared to this point. In conclusion it is noted that neither the overall response nor the maximum load point and the delay of the onset of localization, are affected much by which of the different material length parameters is used. Hence, from now on we will focus on the single parameter theory.

The influence of the amplitude of imperfection is shown in Fig. 6, where the overall responses for both conventional materials (solid curves) and gradient dependent materials (dashed curves) are shown for two different values of the amplitude of the imperfection, namely $\delta_0/a_0 = 5.0 \times 10^{-3}$ (studied until now), and a 10 times smaller initial imperfection, $\delta_0/a_0 = 5.0 \times 10^{-4}$. It is seen that decreasing the imperfection

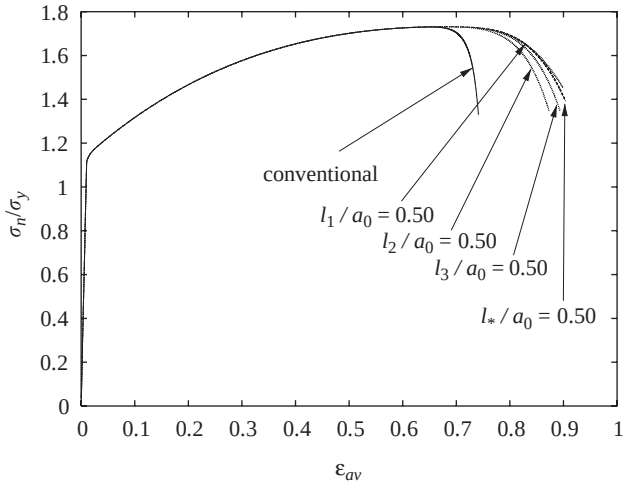

Fig. 5. Overall response for specimens with shear free ends characterized by the geometrical parameters $b_0/a_0 = 3.0$ and $\delta_0/a_0 = 5.0 \times 10^{-3}$, and the material parameters $\sigma_y/E = 0.01$, $\nu = 0.3$, and $E_t/E = 1/40$. The solid curve shows results for a conventional material, the dashed curve shows results for a gradient dependent material with $l_*/a_0 = 0.50$, and the three dotted curves show results for gradient dependent materials modeled by the multi parameter theory with each of the three length parameters l_1, l_2, and l_3 put equal to $a_0/2$ one by one setting the others equal to zero.

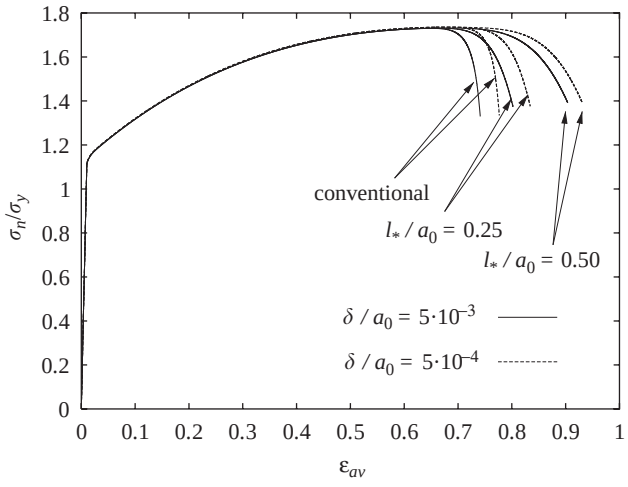

Fig. 6. Overall response for specimens with shear free ends characterized by the geometrical parameters $b_0/a_0 = 3.0$, and the material parameters $\sigma_y/E = 0.01$, $\nu = 0.3$, and $E_t/E = 1/40$. The results are presented for both conventional materials and gradient dependent materials with $l_*/a_0 = 0.25$ and $l_*/a_0 = 0.50$. The solid curves show results for an imperfection of $\delta_0/a_0 = 5.0 \times 10^{-3}$, while the dashed curves show results for $\delta_0/a_0 = 5.0 \times 10^{-4}$.

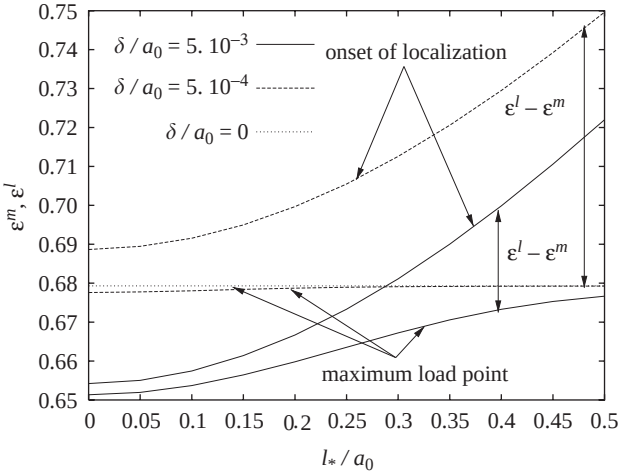

Fig. 7. The strain at the maximum load point and at the onset of localization as a function of the material length parameter, l_*/a_0, for specimens with shear free ends. The aspect ratio is $b_0/a_0 = 3.0$, and the material parameters $\sigma_y/E = 0.01$, $\nu = 0.3$, and $E_t/E = 1/40$. The solid curves show results for a specimen with $\delta_0/a_0 = 5.0 \times 10^{-3}$, and the dashed curves show results for a material with a 10 times smaller imperfection amplitude, $\delta_0/a_0 = 5.0 \times 10^{-4}$. The dotted curve shows the strain at the maximum load point for a specimen without any imperfection.

amplitude results in a right-shift of the part of the response curve that is after the maximum load point, and that this right-shift is rather independent of the value of the material length parameter. For the same two imperfection amplitudes, Fig. 7 shows the maximum strain, ε^{m}, and the strain at the onset of localization, ε^{l}, as a function of the material length parameter l_*/a_0. For the larger imperfection amplitude, the delay of the onset of localization, calculated as $\varepsilon^{\mathrm{l}} - \varepsilon^{\mathrm{m}}$, is 0.003 for a conventional material ($l_* = 0.0$), and it increases with increasing length parameter to 0.045 when $l_*/a_0 = 0.5$. For the smaller imperfection, the delay of the onset of localization is much larger for the conventional material, namely around 0.011, and it increases with increasing l_* to 0.070 when $l_*/a_0 = 0.5$. It is interesting to note in Fig. 7 that the strain at the maximum load point for the large imperfection varies significantly over the range of the material length parameters studied. This strain is below the corresponding curve for the smaller imperfection (which is close to constant), which in turn is below the curve at the maximum load point for a material without any imperfection 0.679. The latter curve is constant as gradient effects are absent in this homogeneous specimen. The figure also shows that decreasing the initial amplitude of the imperfection leads to a delay in the onset of localization, calculated as the difference in strain at the onset of localization for the two different imperfection magnitudes. This delay is rather insensitive to the value of the material length scale, in that it varies from 0.034 for a conventional material to 0.028 for a gradient dependent material with $l_*/a_0 = 0.5$. The stress as a function of the material length parameter at the maximum load point and at the onset of localization, respectively, are shown in Fig. 8. Again, the solid curves

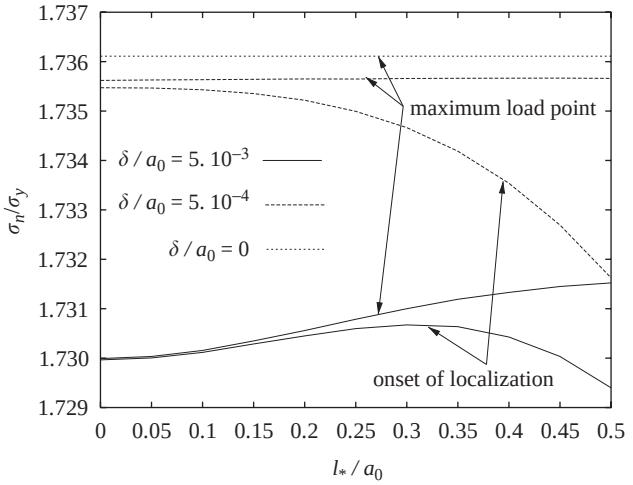

Fig. 8. The stress at the maximum load point and at the onset of localization as a function of the material length parameter, l_*/a_0, for specimens with shear free ends. The aspect ratio is $b_0/a_0 = 3.0$, and the material parameters $\sigma_y/E = 0.01$, $\nu = 0.3$, and $E_t/E = 1/40$. The solid curves show results for a specimen with $\delta_0/a_0 = 5.0 \times 10^{-3}$, and the dashed curves show results for a material with a 10 times smaller imperfection amplitude, $\delta_0/a_0 = 5.0 \times 10^{-4}$. The dotted curve shows the stress at the maximum load point for a specimen without any imperfection.

show results for a specimen with an initial imperfection given by $\delta_0/a_0 = 5.0 \times 10^{-3}$, the dashed curves for $\delta_0/a_0 = 5.0 \times 10^{-4}$, and the dotted constant curve shows the stress at the maximum load point for a specimen without any imperfection. From the figure it is seen that the difference in stress at the maximum load point and at the onset of localization is very small for both non-zero values of the initial imperfection. The figure also illustrates that the maximum stress increases with increasing internal material length scale, since gradient effects become more significant. This tendency is most clear for the larger imperfection, as these specimens have more inhomogeneous deformation fields, and thus more gradient hardening. Although the figure gives interesting qualitative information, the quantitative importance of the trends in the figure is not significant, since all the variations in the figure are well below 1%.

In Fig. 9 the overall response is shown for materials with different tangent moduli and different material length parameters. The three upper curves are characterized by $E_t/E = 1/20$, the three curves in the middle by $E_t/E = 1/40$, and the three lower curves by $E_t/E = 1/60$. The solid curves show results for conventional materials, while the dashed curves show results for gradient dependent materials for two values of l_*/a_0. Comparing the strains, at which the stop criterion is reached, shows that lower hardening specimens are more influenced by the gradient effects than higher hardening specimens. Table 2 shows the strain at maximum load point and at the onset of localization, as well as the delay of the onset of localization for the materials in Fig. 9. It is seen that the delay of the onset of localization decreases with increasing tangent modulus. This means that the delay of the onset of localization decreases with increasing aspect ratio in the

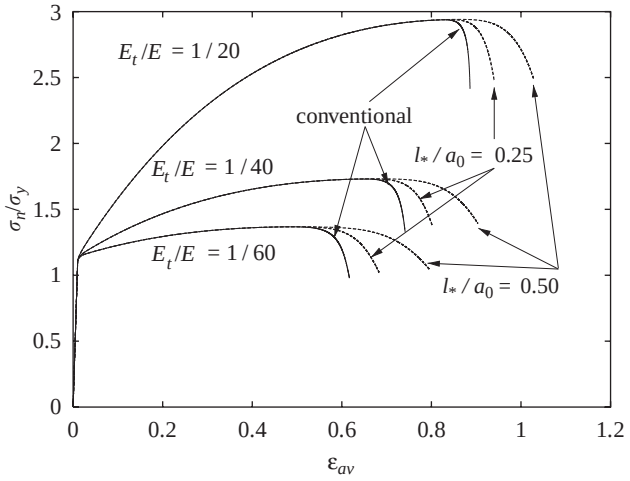

Fig. 9. Overall response for specimens with shear free ends characterized by the geometrical parameters $b_0/a_0 = 3.0$ and $\delta_0/a_0 = 5.0 \times 10^{-3}$, and the material parameters $\sigma_y/E = 0.01$ and $\nu = 0.3$. The solid curves show results for a conventional material, the dashed curves show results for a gradient dependent material with $l_*/a_0 = 0.25$ and $l_*/a_0 = 0.50$. The three different sets of curves show results for different values of the tangent modulus.

Table 2
The average strain at maximum load, ε^{m}, and at the onset of localization, ε^{l}, are shown together with the delay of the onset of localization, $\varepsilon^{\mathrm{l}} - \varepsilon^{\mathrm{m}}$, for conventional materials and different gradient dependent materials, for different values of the tangent modulus

		ε^{m}	ε^{l}	$\varepsilon^{\mathrm{l}} - \varepsilon^{\mathrm{m}}$
$E_t/E = 1/20$	Conventional	0.829	0.830	0.000
	$l_*/a_0 = 0.25$	0.842	0.845	0.003
	$l_*/a_0 = 0.50$	0.861	0.882	0.021
$E_t/E = 1/40$	Conventional	0.651	0.654	0.003
	$l_*/a_0 = 0.25$	0.664	0.673	0.010
	$l_*/a_0 = 0.50$	0.677	0.722	0.045
$E_t/E = 1/60$	Conventional	0.487	0.499	0.012
	$l_*/a_0 = 0.25$	0.495	0.523	0.028
	$l_*/a_0 = 0.50$	0.500	0.583	0.083

The geometry of the specimens is characterized by $b_0/a_0 = 3.0$ and $\delta_0/a_0 = 5.0 \times 10^{-3}$, and the material parameters are $\sigma_y/E = 0.01$, and $\nu = 0.3$. The specimens have shear free ends.

deformed state of the specimen at the maximum load point. This is consistent with the findings in Hill and Hutchinson (1975) for the bifurcation stress, where it is reported that the delay in bifurcation decreases with increasing aspect ratio of the specimen at the maximum load point.

Table 3
The average strain at maximum load, ε^{m}, and at the onset of localization, ε^{l}, are shown together with the delay of the onset of localization, $\varepsilon^{\mathrm{l}} - \varepsilon^{\mathrm{m}}$, for a conventional material and a gradient dependent material for different aspect ratios of the specimen

	ε^{m}	ε^{l}	$\varepsilon^{\mathrm{l}} - \varepsilon^{\mathrm{m}}$
$b_0/a_0 = 2$, (conv.)	0.667	0.683	0.016
$b_0/a_0 = 3$, (conv.)	0.651	0.654	0.003
$b_0/a_0 = 4$, (conv.)	0.642	0.643	0.001
$b_0/a_0 = 2$, $(l_*/a_0 = 0.5)$	0.679	0.804	0.125
$b_0/a_0 = 3$, $(l_*/a_0 = 0.5)$	0.677	0.722	0.045
$b_0/a_0 = 4$, $(l_*/a_0 = 0.5)$	0.669	0.686	0.016

The amplitude of the imperfection is $\delta_0/a_0 = 5.0 \times 10^{-3}$, and the conventional material parameters are $\sigma_y/E = 0.01$, $\nu = 0.3$, and $E_{\mathrm{t}}/E = 1/40$. The specimens have shear free ends.

Table 3 shows ε^{m}, ε^{l}, and $\varepsilon^{\mathrm{l}} - \varepsilon^{\mathrm{m}}$, for a conventional material and a gradient dependent material ($l_*/a_0 = 0.50$) for different aspect ratios of the specimen in the undeformed geometry b_0/a_0. The table shows that, in accordance with the findings of Needleman (1972) and Hill and Hutchinson (1975) for conventional materials and Benallal and Tvergaard (1995) for gradient dependent materials, the delay in onset of localization decreases with increasing aspect ratio of the specimen. Furthermore, the table shows that the delay is significantly larger for the gradient dependent materials than for the conventional materials for all values of the aspect ratio.

Until now we have studied specimens with shear free ends. A problem which is perhaps easier to study experimentally is tension of a specimen with rigid grips at the ends, so that the specimen cannot contract in the directions orthogonal to the tensile direction at the ends. For this type of loading no initial imperfection is needed for a neck to develop. Fig. 10 shows the overall stress–strain response for specimens with rigid grips both for a conventional material and for two gradient dependent materials. For comparison the response curve for the conventional material with shear free ends (from Fig. 2) is also shown in this figure. All specimens have an initial aspect ratio of $b_0/a_0 = 3$, and a tangent modulus of $E_{\mathrm{t}}/E = 1/40$. It is seen that although the specimens with rigid grips behave stiffer to begin with, due to the increased constraint at the ends, localization sets in earlier, and this leads to a softer response at larger strains, when compared to specimens with shear free ends. In Fig. 11 the amplitude of the neck is shown as a function of average strain for the specimens discussed in Fig. 10. The figure shows that for the rigid grips, the amplitude of the neck increases significantly from the beginning of the deformation, which is not the case for the specimen with shear free ends. Furthermore, it is seen that while gradient hardening decreases the neck amplitude for large strains, the neck increases slightly with increasing material length l_* in the beginning of the deformation (before the onset of localization).

The deformed meshes at the end of the numerical simulations are shown in Fig. 12 together with the undeformed meshes and the active plastic zones, which are marked by the black areas in the necks. This figure illustrates that increasing gradient hardening

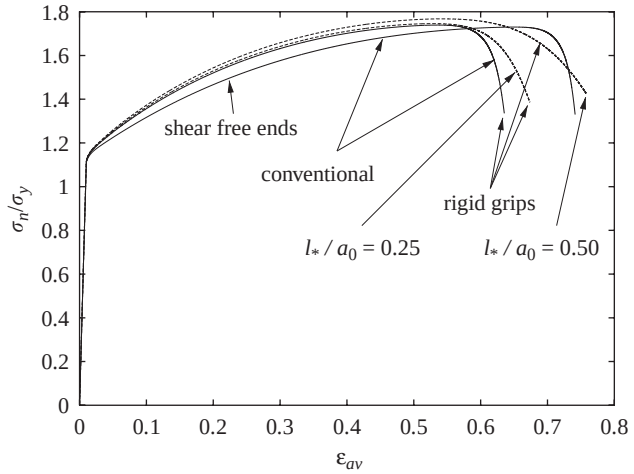

Fig. 10. Overall response for specimens with rigid grips. The geometrical parameters are $b_0/a_0 = 3.0$ and $\delta_0/a_0 = 5.0 \times 10^{-3}$, and the material parameters $\sigma_y/E = 0.01$, $\nu = 0.3$, and $E_t/E = 1/40$. The solid curve shows results for a conventional material, while the two dashed curves show results for materials with $l_*/a_0 = 0.25$ and $l_*/a_0 = 0.50$. For comparison the stress–strain curve for a conventional material with shear free ends is shown in the figure.

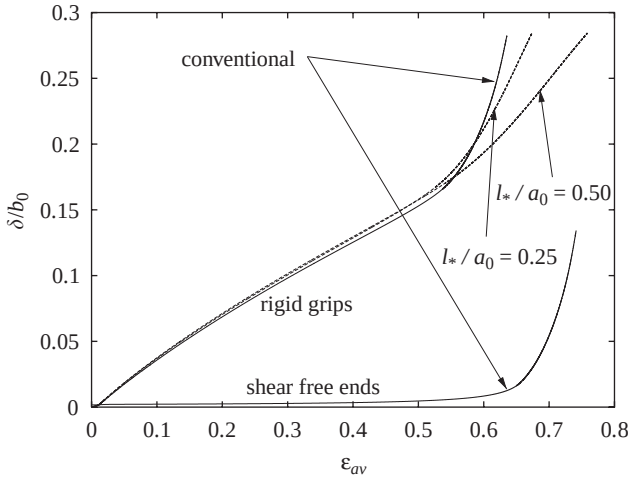

Fig. 11. Development of the neck for specimens with rigid grips. The specimen is characterized by the aspect ratio $b_0/a_0 = 3.0$, and the material parameters $\sigma_y/E = 0.01$, $\nu = 0.3$, and $E_t/E = 1/40$. The solid curve shows results for a conventional material, while the two dashed curves show results for materials with $l_*/a_0 = 0.25$ and $l_*/a_0 = 0.50$. For comparison the corresponding curve for a conventional material with shear free ends is shown in the figure.

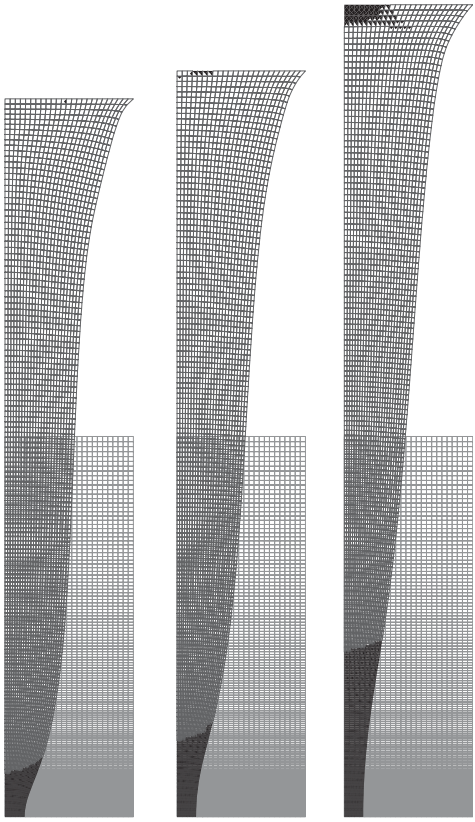

Fig. 12. Deformed geometries at the end of the simulations for specimens with rigid grips. The geometry is characterized by the initial aspect ratio $b_0/a_0 = 3.0$, and the material is characterized by the parameters $\sigma_y/E = 0.01$, $\nu = 0.3$, and $E_t/E = 1/40$. Figure (a) shows the deformed geometry for a conventional material, and figures (b) and (c) show the deformed geometries for gradient dependent materials with $l_*/a_0 = 0.25$ and $l_*/a_0 = 0.50$, respectively. The black areas show the zones that are being plastically loaded, while the rest is being elastically unloaded.

increases the length of the neck zone, and hence the deformations are less localized; conclusions which are the same as those of Fig. 3, where results for specimens with shear free ends were discussed.

5. Conclusion

A finite strain version of the strain gradient plasticity theory by Fleck and Hutchinson (2001a) has been proposed. The formulation has been used to study size-effects in plane strain sheet-necking at average logarithmic strains up to around 1.

Introducing gradient effects in the necking problem results in attaining the onset of localization at larger overall strains. Before reaching the maximum load point, the stress state is almost homogeneous, hence the stress–strain response prior to the maximum load is almost independent of whether or not a material length scale is included. The delay between maximum load and onset of localization is increased with increasing influence of strain gradients. The size of the plastic zone in the neck is larger when $l_*/a_0 > 0$ compared to the necking behavior in a conventional material. Furthermore, it has been shown that the multi parameter theory and the single parameter theory for the present problem lead to qualitatively the same results.

A larger material length scale leads to wider shear bands at a given overall strain as reported by Sluys and Estrin (2000). Similarly, in the present study the gradient effects are found to depress localization, in that they lead to smaller neck amplitudes.

Different imperfection amplitudes have been tested and it has been found that a smaller imperfection leads to larger overall strains at the maximum load and later onset of localization, both for the conventional material and the gradient dependent materials. The delay from the maximum load to the onset of localization is also increased with decreased imperfection amplitude.

Stress–strain responses for different degrees of hardening (different tangent moduli) have been studied as well. The gradient hardening contributions are more important for the lower hardening specimens. Moreover, the strain levels at maximum load and at the onset of localization are significantly higher with increasing tangent modulus, hence, the relative gradient hardening is larger for the lower values of E_t/E.

In the numerical analyzes with rigid grips at the ends of the specimen, no imperfection is necessary to trigger localization. The stress–strain response when the ends are fixed is stiffer in the beginning of the tensile test, but the maximum load and the onset of localization are reached earlier compared to the specimens with shear free ends. The neck amplitudes are much larger for the rigid grips results compared to the amplitudes where the material is free to contract at the ends.

The focus of the present work on linear hardening and relative high hardening materials leads to rather large localization strains. A more low hardening material would give rupture of the sheet at smaller strains. For a power law hardening material response or lower hardening in general, localization will occur at smaller strains in closer agreement with experimental data (see e.g. Huang and Spaepen, 2000; Espinosa et al., 2003), but a different numerical procedure from the one used in this work is then necessary. We are currently working on a different numerical implementation of the method that will make it possible to also obtain good convergence for power law hardening materials and materials with even lower linear hardening than presented in this study.

Acknowledgements

This work was supported by the FREJA research project, Application of Advanced Material Models in the Analysis of Metal Forming Processes, financed by the Danish Research Agency. The authors would like to thank professors John W. Hutchinson and

Norman A. Fleck for sharing their unpublished work on the strain gradient plasticity theory. Professors Viggo Tvergaard, Alan Needleman, and Ann Bettina Richelsen are acknowledged for their inspiration and many helpful discussions.

References

Acharya, A., Bassani, J.L., 1996. On non-local flow theories that preserve the classical structure of incremental boundary value problems. In: Pineau, A., Zaoui, A. (Eds.), IUTAM Symposium on Micromechanics of Plasticity and Damage of Multiphase Materials. Kluwer Academic Publishers, Dordrecht, pp. 3–9.

Aifantis, E.C., 1984. On the microstructural origin of certain inelastic models. Trans. ASME: J. Eng. Mater. Technol. 106 (4), 326–330.

Bassani, J.L., 2001. Incompatibility and a simple gradient theory of plasticity. J. Mech. Phys. Solids 49, 1983–1996.

Begley, M.R., Hutchinson, J.W., 1998. Mechanics of size-dependent indentation. J. Mech. Phys. Solids 46 (10), 2049–2068.

Benallal, A., Tvergaard, V., 1995. Nonlocal continuum effects on bifurcation in the plane strain tension-compression test. J. Mech. Phys. Solids 43 (5), 741–770.

de Borst, R., Mühlhaus, H.-B., 1992. Gradient-dependent plasticity: formulation and algorithmic aspects. Int. J. Numer. Methods Eng. 35, 521–539.

de Borst, R., Pamin, J., 1996. Some novel developments in finite element procedures for gradient-dependent plasticity. Int. J. Numer. Methods Eng. 39, 2477–2505.

Deshpande, V., Needleman, A., Van der Giessen, E., 2003. Finite strain discrete dislocation plasticity. J. Mech. Phys. Solids 51, 2057–2083.

Espinosa, H.D., Prorok, B.C., Fischer, M., 2003. A methodology for determining mechanical properties of freestanding thin films and mems materials. J. Mech. Phys. Solids 51, 47–67.

Fleck, N.A., Hutchinson, J.W., 1997. Strain gradient plasticity. In: Hutchinson, J.W., Wu, T.Y. (Eds.),, Advances in Applied Mechanics, Vol. 33. Academic Press, New York, pp. 295–361.

Fleck, N.A., Hutchinson, J.W., 2001a. A reformulation of strain gradient plasticity. J. Mech. Phys. Solids 49, 2245–2271.

Fleck, N.A., Hutchinson, J.W., 2001b. A working paper on strain gradient plasticity theory.

Fleck, N.A., Muller, G.M., Ashby, M.F., Hutchinson, J.W., 1994. Strain gradient plasticity: theory and experiment. Acta Metall. Mater. 42 (2), 475–487.

Gurtin, M.E., 2002. A gradient theory of single-crystal viscoplasticity that accounts for geometrically necessary dislocations. J. Mech. Phys. Solids 50, 5–32.

Hill, R., Hutchinson, J.W., 1975. Bifurcation phenomena in the plane tension test. J. Mech. Phys. Solids 23, 239–264.

Huang, H., Spaepen, H., 2000. Tensile testing of free standing cu, ag, and al thin films and ag/cu multilayers. Acta Mater. 48, 3261–3269.

Hutchinson, J.W., 2000. Plasticity at the micron scale. Int. J. Solids Struct. 37, 225–238.

Hwang, K., Jiang, H., Huang, Y., Gao, H., 2003. Finite deformation analysis of mechanism-based strain gradient plasticity: torsion and crack tip field. Int. J. Plasticity 19, 235–251.

McMeeking, R.M., Rice, J.R., 1975. Finite-element formulations for problems of large elastic-plastic deformation. Int. J. Solids Struct. 11, 601–616.

Needleman, A., 1972. A numerical study in circular cylindrical bars. J. Mech. Phys. Solids 20, 111–127.

Niordson, C.F., Hutchinson, J.W., 2003a. Non-uniform plastic deformation of micron scale objects. Int. J. Numer. Methods Eng. 56, 961–975.

Niordson, C.F., Hutchinson, J.W., 2003b. On lower order strain gradient plasticity theories. Eur. J. Mech. A/Solids 22, 771–778.

Niordson, C.F., Tvergaard, V., 2002. Nonlocal plasticity effects on fibre debonding in a whisker-reinforced metal. Eur. J. Mech. A/Solids 21, 239–248.

Sluys, L., Estrin, Y., 2000. The analysis of shear banding with a dislocation based gradient plasticity model. Int. J. Solids Struct. 37, 7127–7142.

Stölken, J.S., Evans, A., 1998. A microbend test method for measuring the plasticity length scale. Acta Mater. 46 (14), 5109–5115.

Tvergaard, V., Niordson, C.F., 2004. Nonlocal plasticity effects on interaction of different size voids. Int. J. Plasticity 20, 107–120.

Vardoulakis, I., Aifantis, E., 1991. A gradient flow theory of plasticity for granular materials. Acta Mech. 87, 197–217.

Wei, Y., Hutchinson, J.W., 1997. Steady-state crack growth and work of fracture for solids characterized by strain-gradient plasticity. J. Mech. Phys. Solids 45 (8), 1253–1273.

Yamada, Y., Sasaki, M., 1995. Elastic-plastic large deformation analysis program and lamina compression test. Int. J. Mech. Sci. 37, 691–707.